ABCM 40 anos
Associação Brasileira de Engenharia e Ciências Mecânicas

CONEM 2016
CONGRESSO NACIONAL DE ENGENHARIA MECÂNICA

21 - 25
AGOSTO DE 2016
FORTALEZA - CEARÁ

Design and optimization of a bias SMA flap actuator in a fluid-structure application

Pedro Batista Camara Leal, leal2608@poli.ufrj.br[1]
Marcelo Amorim Savi, savi@mecanica.coppe.ufrj.br[1]

[1]Universidade Federal do Rio de Janeiro, COPPE – Department of Mechanical Engineering, Center for Nonlinear Mechanics, Rio de Janeiro – RJ – Brazil – 21.945.970 – P.O. Box 68.503

Abstract: *As an effort to create efficient and lighter flap actuators via the use of shape memory alloy actuators (SMA), the main objective of this work is to demonstrate the viability and capability of SMA wires as flap actuators in a bias configuration. Numerical modeling via a Hartl-Lagoudas constitutive model of the SMA actuators is undertaken. The flap is modeled by a static rigid-body with a single actuator under aerodynamic loads calculated via panel method in a fluid-structure-interaction framework. Elastic spring properties, pre-strain, positioning of the actuators and final actuation temperature are optimized via a genetic optimization for two different problems. The first optimization focuses on maximizing the trailing edge displacement. The second optimization also maximizes the flap deflection, but also minimizes the bias spring coefficient in order to have a more realistic actuator. Each optimization is implemented and significant flap deflections are obtained.*
Keywords: *shape memory alloys, fluid-structure interaction, dynamics, optimization*

1. INTRODUCTION

Aircraft wings are designed to have high performance during the flight condition that represents the majority of flight time, cruise. For other conditions, mechanisms are implemented to modify the wing geometry and, as a result, the aerodynamic properties. The high-lift devices such as flaps and slats are a category of these mechanisms implemented to increment lift during various flight conditions (Anderson, 2011). As an essential aircraft component, flap actuators are compact, have a high fatigue life and are able to exert high forces. Traditional materials used in the industry utilize materials with linear properties, e.g. constant rate between deformation and force, that facilitate their application. To exceed the limitations of modern actuators built out of traditional materials, new materials are necessary.

Among these non-traditional components, smart material actuators are an interesting option to further improve flap performance. Because these actuators usually have non-linear properties and sometimes unpredictable performance, the industry has not yet integrated them. Notwithstanding, researchers have thoroughly analyzed and modeled smart materials for the last few decades (Lagoudas, 2008). It is the authors' belief that the level of technology for some of these smart materials is now mature enough to develop new and realistic aerospace applications. A possible application for flap technology is to substitute pneumatic mechanisms for the compact and high-performance smart material actuators.

Compared to other smart materials (e.g. piezoelectric, shape memory polymers and others), SMA components (e.g. wires, springs and ribbons) have high actuation stress, high actuation strain and thus high energy density (Hartl and Lagoudas, 2007). The main challenges for SMA implementation include energy efficiency and functional fatigue (Barbarino *et al.*, 2014), i.e. the loss of actuation stroke over a number of cycles. Although functional fatigue is a serious mechanical problem, Kumar and Lagoudas (Lagoudas, 2008) have reported that thermally-induced partial martensitic transformations cycles significantly extend the material's fatigue life. Therefore, for applications with low frequency such as flaps and high force requirements, SMA actuators are suited. Although the material has non-linear properties, several reliable constitutive models have been developed and validated for this purpose. Lagoudas *et al.* (2012) and Paiva and Savi (2006) presented a general overview of these models.

Several works have proposed the use of SMA actuators for the development of morphing structures (Barbarino *et al.*, 2014; Camara Leal *et al.*, 2015). However, the complexity of such mechanisms impedes their experimental validation. Others have applied SMA wires as actuators for control surfaces (Senthilkumar, 2012; Kudva, 2004), but several works (Song *et al.*, 2000; Senthilkumar, 2012; Enemark *et al.*, 2014) concluded that wires can be quite limiting for flap deflections. At the cost of providing less force, higher strokes are achieved with SMA springs. Regardless if wires or spring are utilized, SMA actuators utilizing the shape memory effect (SME) to achieve motion are classified as either *bias* or *antag-*

onistic. A bias configuration consists of one SMA actuator acting against one bias spring. It is characterized as having larger stroke, fast actuation during heating, but slow reset during cooling (Donnelan, 2005). An antagonistic configuration consists of a pair of SMA actuators arranged antagonistically. Because one can control the motion in both directions actively, it has enhanced controllability (Ikuta *et al.*, 1988). Thus, applications focusing on control tend to be antagonistic (Moallem and Tabrizi, 2009; Ikeda *et al.*, 2015; Faria, 2010; Abreu, 2012).

Inspired by prototypes found in the literature for bias configuration (Bellini *et al.*, 2009; Elahinia and Ashrafiuon, 2002), a bias mechanism of two actuators, a passive elastic spring and an SMA wire, actuated by heating is utilized. The flap itself acts as a lever for magnifying the displacement for the SMA components which are modeled via the constitutive model from Lagoudas *et al.* (2012). The use of a wire is of interest because of the high force necessary in an aircraft flap. To minimize the effects of a small stroke, the actuators are optimized utilizing two different cost functions. The first focuses only in obtaining greater flap deflection, while the second focuses on obtaining an actuator with low stiffness for the bias spring and high flap deflection.

The paper is organized in the following fashion: the governing equation and the constraints of the rigid-body flap are thoroughly described in section 2; the numerical procedure, optimization results and the performance of the optimized design are presented in section 3; and the conclusions are made in section 4.

2. MATHEMATICAL MODEL

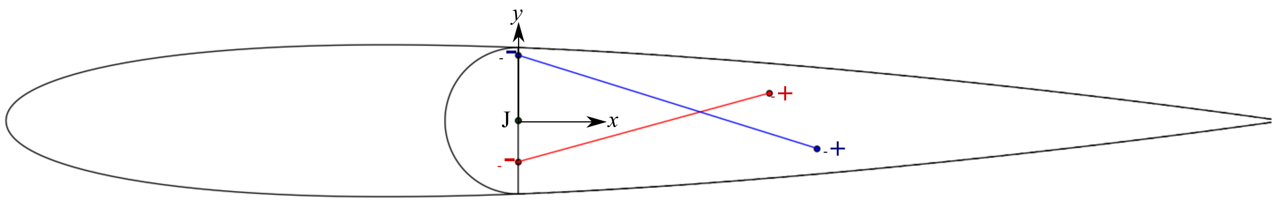

Figure 1: Schematic of the bias spring mechanism (SMA wire in red and elastic spring in blue) with exaggerated flap size for better illustrating the design.

There are several airfoil designs that establish different efficiency, some examples are single-slotted flap, double-slotted flap and split flap (Schmidt, 2012). Here, a plain flap geometry is utilized as schematically illustrated in figure 1, where the actual flap chord is 25% of the wing chord. Although a simple design, it has the same challenges of a more complex flap. The mechanism consists of an elastic bias spring and a martensitic SMA wire annexed to isolating fixtures. The linear spring stiffness coefficient, k, must be high enough so that the SMA actuator is fully detwinned in order to obtain the maximum stroke possible. Since the flap components are subject to low stresses, these components are herein modeled as rigid bodies. Moreover, the transient response of the system is not of interest; hence the problem is statically modeled and the inertia components are neglected. Figure 1 shows that one end of the actuator, point $-$, is fixed on the forwards component, while the other, point $+$, is connected to the afterwards component. The actuators can cross each other because they are considered to be in different planes parallel to the airfoil plane. The two rigid bodies are connected at the joint point J.

Before stating the governing equation, it is necessary to define the direct and inverse kinematics of the problem.

2.1 Kinematics

As can be noticed in figure 2, both actuators have the same geometric and kinematic properties; hence the subscript i is used to denote that all equations in this section are valid for both actuators. Since the distance between two points on the same rigid-body is constant, the position vector ${}_I\mathbf{r}_i^-$ connecting the joint to forwards point $-$ is constant in the inertial reference system I and the position vector ${}_I\mathbf{r}_i^+$ connecting the joint to afterwards point $+$ is constant in the reference frame R auxiliary to the rotated reference system. Therefore, the position vectors are:

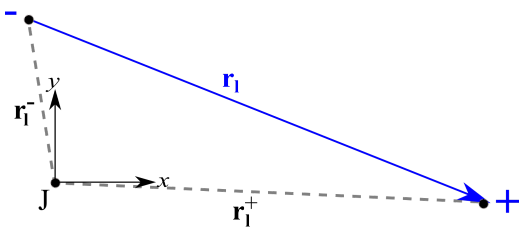

(a) Linear actuator.

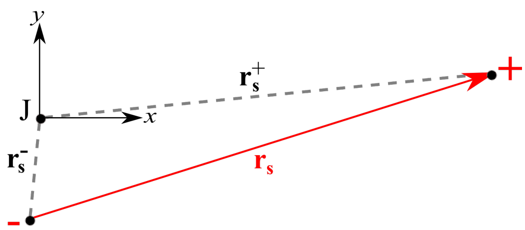

(b) SMA actuator.

Figure 2: Schematics of both actuators (linear and SMA).

$$ {}_{I}\mathbf{r}_i^- = \begin{pmatrix} x_i^- \\ y_i^- \\ 0 \end{pmatrix} \quad {}_{R}\mathbf{r}_i^+ = \begin{pmatrix} x_i^+ \\ y_i^+ \\ 0 \end{pmatrix} \tag{1} $$

As in the work from Faria (2010) the force $\mathbf{F}_i$ generated by each actuator has magnitude F_i which is determined by the constitutive model and the same direction as the actuator position vector $\mathbf{r}$, i.e. the distance between points $+$ and $-$. Thus:

$$ {}_{I}\mathbf{F}_i = -\frac{{}_{I}\mathbf{r}_i}{||\mathbf{r_i}||}F_i \quad \text{where,} \quad {}_{I}\mathbf{r}_i = \begin{pmatrix} x_i^r \\ y_i^r \\ 0 \end{pmatrix} = {}_{I}\mathbf{r}_i^+ - {}_{I}\mathbf{r}_i^- \tag{2} $$

If θ is the rotation angle around joint point J, ${}_{I}T_R$ is the rotation transformation from reference frame R to I, and $\{x_J, y_J, 0\}$ are coordinates of J, the vector ${}_{R}r_i^+$ in the inertial reference system is given by:

$$ {}_{I}\mathbf{r}_i^+ = {}_{I}T_{RR}\mathbf{r}_i^+ = \begin{bmatrix} \cos\theta & -\sin\theta & 0 \\ \sin\theta & \cos\theta & 0 \\ 0 & 0 & 1 \end{bmatrix} \begin{pmatrix} x_i^+ \\ y_i^+ \\ 0 \end{pmatrix} = \begin{pmatrix} x_i^+\cos\theta - y_i^+\sin\theta \\ x_i^+\sin\theta + y_i^+\cos\theta \\ 0 \end{pmatrix} \tag{3} $$

From equation 2, the direct kinematic solution for the position vector $\mathbf{r}_i$ in the inertial reference system is:

$$ {}_{I}\mathbf{r}_i = \begin{pmatrix} x_i^+\cos\theta - y_i^+\sin\theta - x_i^- \\ x_i^+\sin\theta + y_i^+\cos\theta - y_i^- \\ 0 \end{pmatrix} \tag{4} $$

For direct kinematics, the position vector $\mathbf{r}_i$ is an analytic function of the deflection θ, but for a problem of inverse kinematics, the deflection angle θ can only be numerically estimated as a function of a given strain ϵ_i of the actuator. If the length of the actuator $||\mathbf{r}_i||$ undergoes a strain ϵ_i, which translated into a deformation $\eta_i = 1 + \epsilon_i$, and the initial actuator length is $||\mathbf{r}_o||$, the resultant angle θ has to solve the following equality:

$$ \eta_i||\mathbf{r}_{i,o}|| = ||\mathbf{r}_i|| = \sqrt{({}_{R}x_i^r)^2 + ({}_{R}y_i^r)^2} \tag{5} $$

$$ \eta_i||\mathbf{r}_{i,o}|| = \sqrt{(x_i^+\cos\theta - y_i^+\sin\theta - x_i^-)^2 + (x_i^+\sin\theta + y_i^+\cos\theta)^2} \tag{6} $$

$$ 0 = \sqrt{(x_i^+\cos\theta - y_i^+\sin\theta - x_i^-)^2 + (x_i^+\sin\theta + y_i^+\cos\theta)^2} - \eta_i||\mathbf{r}_{i,o}|| \tag{7} $$

For a stress-free state, the actuator has length L_i, i.e. the length of the actuator before coupling to the flap structure. If L_i is not equal to the magnitude of vector $\mathbf{r}_i$, the actuator is deformed at initial conditions. If $L_i > \mathbf{r}_i$, the actuator is stretched. If $L_i < \mathbf{r}_i$, the actuator is compressed. Taking into consideration this initial deformation, the deformation η_i at any given instance and the initial strain $\epsilon_{i,o}$ are:

$$ \eta_i = 1 + \epsilon_i - \epsilon_{i,o} \tag{8} $$

$$ \epsilon_{i,o} = \frac{||{}_{I}\mathbf{r_i}||}{L_i} - 1 \tag{9} $$

2.2 Governing equation

Since the flap is a one degree of freedom system, the governing equation is defined by static moment equilibrium, where all inertial phenomena are neglected. Denoting dimensions and properties of the shape memory alloy actuators with subscript s, linear actuators with subscript l, the weight with subscript w and aerodynamic pitching moment with a; the governing equation is:

$$ \tau_s(\epsilon_s) + \tau_l(\epsilon_s) + \tau_w(\epsilon_s) + \tau_a(\epsilon_s) = 0 \tag{10} $$

where each torque τ is generated by: the SMA actuator (τ_s), the linear actuator (τ_l), weight (τ_w) and the resultant aerodynamic loads (τ_a). As depicted in the equation, it is possible to formulate all the torques as a function of unique variable, the SMA actuator deformation ϵ_s. Considering that the deflection θ is calculated as a function of ϵ_s via equation 7, the formulation of each torque is as follows:

- τ_s: the torque provided by the SMA actuator is given by ${}_{I}\mathbf{r}_s^+ \times {}_{I}\mathbf{F}_s$. Since stress σ_s is obtained from the constitutive equations from the Lagoudas model (Lagoudas *et al.*, 2012) and A is the cross-section area of the wire, the force generated by the SMA actuator is $F_s = \sigma_s A$ and the torque τ_s is:

$$ \tau_s = \frac{\sigma_s A}{||\mathbf{r_s}||}\left[(x_s^+\sin\theta + y_s^+\cos\theta)x_{s,o}^r - (x_s^+\cos\theta - y_s^+\sin\theta)y_{s,o}^r\right] \tag{11} $$

- τ_l: the torque generated by the linear actuator is given by ${}_I\mathbf{r}_l^+ \times {}_I\mathbf{F}_l$. The force F_l in regards to the strain ϵ_l is linear, e.g. $F_l = k\epsilon_l||\mathbf{r_l}||$. Thus,

$$\tau_l = k\epsilon_l \left[(x_l^+ \sin\theta + y_l^+ \cos\theta) x_{l,o}^r - (x_l^+ \cos\theta - y_l^+ \sin\theta) y_{l,o}^r \right] \tag{12}$$

If $\mathbf{r}_l$ is given by equation 4 and L_l is the the length of the linear actuator at the stress-free state, the strain of the linear actuator is:

$$\epsilon_l = \frac{||\mathbf{r}_l||}{L_l} - 1 \tag{13}$$

- τ_w: the weight driven torque is generated by the cross product of the weight which is always vertical and the distance vector from the joint to the center of gravity. If W is a scalar that depicts the flap weight and r_w is the distance from the joint to the center of gravity, the torque τ_w is:

$$\tau_w = -r_w W \cos\theta \tag{14}$$

- τ_a: the resultant aerodynamic torque is:

$$\tau_a = -c_{m,J} \rho V_\infty^2 c^2 \tag{15}$$

where $c_{m,J}$ is the two-dimensional moment coefficient at the joint, ρ is the air density, V_{inf} is the aircraft velocity and c is the chord. A panel method (Drela, 2001) is implemented via the AeroPy (Camara Leal, 2016) interface to calculate the discrete distribution of pressure coefficients c_p on the airfoil surface. The trapezoid rule (Ruggiero and Lopes, 1996) is used to calculate the resultant force at the center of each panel as depicted in figure 3. Calculating the moment coefficient for each panel based on the resultant force and summing all of the moment coefficients, the total moment coefficient is:

$$\begin{aligned} c_{m,J} = \sum_{i=0}^{n-1} \frac{c_p(x_i) + c_p(x_{i+1})}{2} \Bigg[& (x_i - x_{i-1}) \left(\frac{x_i + x_{i+1}}{2} - x_J \right) \\ & + (y_i - y_{i-1}) \left(\frac{y_i + y_{i+1}}{2} - y_J \right) \Bigg] \end{aligned} \tag{16}$$

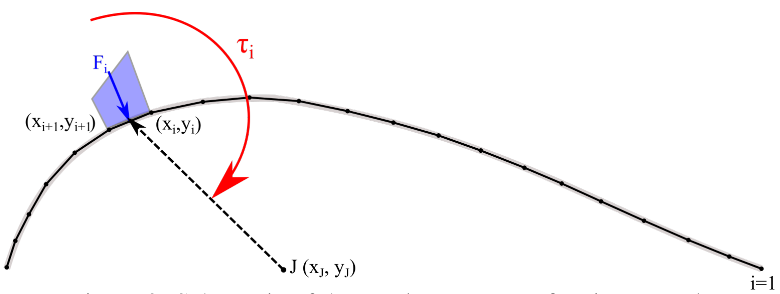

Figure 3: Schematic of the resultant torque of a given panel.

2.3 Kinematic constraints

Because of physical or actuation limitations, certain parameters are constrained or must satisfy certain criteria. To simplify the initial conditions, the SMA pre-tension is considered constant and the wire/spring outer diameters are not taken into consideration when applying constraints. During the simulation, the temperature increases the deflection θ up to the maximum deflection. At any given moment, the actuators cannot cross the joint J. Such a constraint exists, because the torque of the actuator crossing J is generating zero torque. In this section, other constraints such as the maximum deflection and other initial conditions are introduced.

Maximum deflection (θ_{max}): because of feasibility constraints, the flap deflection has two geometric restrictions which are depicted in figure 4. For each restriction, the maximum deflection at which the restraint is not violated is calculated and the smallest of the two is utilized as the static simulation maximum deflection.

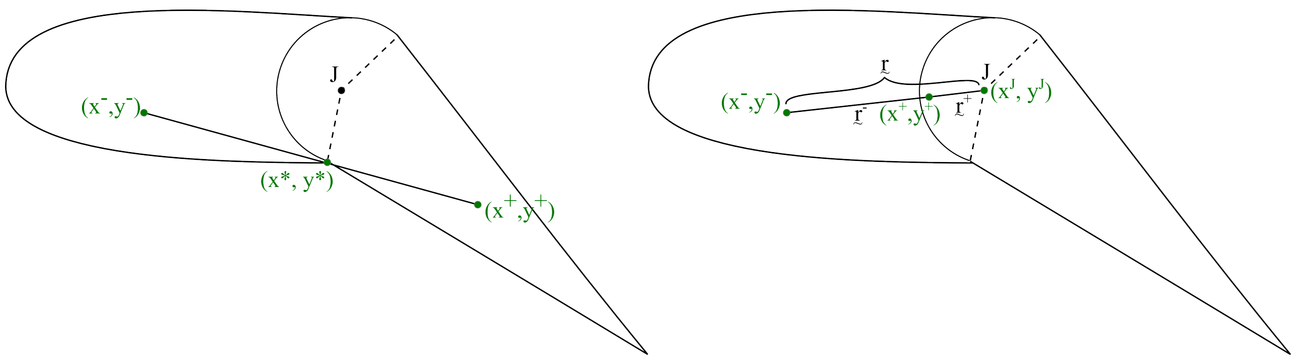

(a) θ_A. (b) θ_B.

Figure 4: Schematics of constraining configurations.

Initial transformation strain ($\epsilon^t_{s,o}$): At initial conditions, $\theta = 0$, the temperature is below transformation temperature; hence it is expected that the shape memory alloy actuator is fully martensitic. Considering the initial pre-stress as a parameter, from the relation of transformation strain in function of stress (Lagoudas *et al.*, 2012), for $\sigma_{s,o} > \sigma_{crit}$ (σ_{crit} is the stress at which transformation starts) the following is valid:

$$\epsilon^t_{s,o} = H_{min} + (H_{max} - H_{min})\left(1 - e^{-k(\sigma_o - \sigma_{crit})}\right) \tag{17}$$

where H_{min} is the minimum transformation strain, H_{max} describes the ultimate transformation strain and k controls the rate at which the transformation evolves from H_{min} to H_{max}.

SMA actuator pre-strain ($\epsilon_{s,o}$): Since, this main objective of this work is the development of a reusable actuator device, it is necessary that after heating the SMA actuator, the original configuration is attained after cooling. Since a fully detwinned martensite has linear elastic properties, the initial strain is:

$$\epsilon_{s,o} = \frac{\sigma_o}{E_M} + \epsilon^t_{s,o} \tag{18}$$

SMA actuator length (l_s): Since the SMA is a wire, it is easy to change the actuator length. Therefore, the length of the wire is such that it provides the required strain $\epsilon_{s,o}$ for a given actuator $\mathbf{r}_s$, hence:

$$l_s = \frac{||\mathbf{r}_s||}{1 + \epsilon_{s,o}} \tag{19}$$

Linear actuator stiffness (k) To ensure that after cooling the strain is equal to the initial SMA strain $\epsilon_{s,o}$, the linear actuator must provide sufficient stress to fully detwine the martensitic actuator. Thus, the spring stiffness k is such that the governing equation (eq. 10) is satisfied at $\theta_o = 0$; hence from equation 10 and 12:

$$k = -\frac{\tau_s + \tau_a + \tau_w}{\epsilon_l\left[y^+_l x_{r,o} - x^+_l y_{r,o}\right]} \tag{20}$$

3. NUMERICAL RESULTS

In this work two optimizations are undertaken. The first optimization focuses in increasing the flap deflection without restrictions to the linear actuator stiffness. This step calculates the maximum deflection possible without violating any of the kinematic constraints (subsection 2.3). The second optimization focuses in increasing the flap deflection while simultaneously minimizing the linear actuator stiffness k. The requirement of a lower stiffness should result in more realistic designs.

For both problems, a non-sorted genetic algorithm known as NSGA-2 (Deb *et al.*, 2002) is utilized. Genetic algorithms consider each analyzed configuration as an individual and all the individuals of a given iteration/generation are known as the population. Through the use of evolution inspired mechanisms (crossover, mutation and survival of the fittest) the best solution is found. All the algorithm parameters herein used are the default values of the library (Perez *et al.*, 2012) expect for the number of generation, 50, and the population size, 40. To minimize the number of design variables, certain values are held constant (table 1). The SMA properties are from a equiatomic NiTi from the work of Lagoudas *et al.* (2012). Furthermore, the domains of each design variable are defined in table 2.

The static simulation procedure is temperature driven. Therefore, at each step of the simulation, the temperature is increased. For each temperature, the solution of the governing equation is calculated via Brent's Method. The constitutive

Table 1: All constant parameters.

Variable	Value
Angle of attack α	0
Altitude	300 m
Chord c	1 m
Coordinate x_J	0.75 m
Coordinate y_J	0 m
Flap center of gravity	0.85 m
Velocity V_∞	10 m/s
Pre-tension σ_o	400 Mpa
Linear stress-free length L_l	0.1 m
Initial temperature T_o	200 K
Maximum temperature T_{max}	400 K
Flap weight W	1.96 N
SMA wire radius	.25 mm

Table 2: Design variable domains.

$-x_J/2$	$\leq x_s^- \leq$	0
-0.9	$\leq \bar{y}_s^- \leq$	0
0	$\leq x_s^+ \leq$	$0.95c - x_J$
0	$\leq \bar{y}_s^+ \leq$	0.9
$-x_J/2$	$\leq x_l^- \leq$	0
-0.9	$\leq \bar{y}_l^- \leq$	0.9
0	$\leq x_l^+ \leq$	$0.95c - x_J$
-0.9	$\leq \bar{y}_l^+ \leq$	0.9

modeling of the SMA wires is accomplished via a MATLAB code created by the Texas Institute for Intelligent Materials and Structures (TiiMS). Because this is also a Fluid-Structure Interaction (FSI) problem, the aerodynamic moment τ_a is calculated at each iteration via the AeroPy interface (Camara Leal, 2016).

3.1 Deflection optimization

This first optimization only focuses in increasing the deflection θ; hence, there is only one objective function. Because of the reference frame utilized, a clockwise rotation results in negative angles. Therefore, to increase the magnitude of the flap deflection, it is necessary to minimize it. This definition is convenient because optimization algorithms are usually developed for minimizing a giving cost function. As such, the cost function for this first optimization C_1 is the deflection; hence:

$$C_1 = \theta \tag{21}$$

Following the numerical model for the static simulation and the optimization, the cost function (eq. 21) is optimized. All of the individuals/configurations analyzed in the optimization, their cost and generation number are depicted in figure 5. In the first thirty generations, there is a considerable increase of θ and most individuals in the population follow the same trend. However, after thirty generation, there are small improvements. Because this is a genetic algorithm, mechanisms such as mutation enables the optimizer to explore regions not close to the best individual in order to avoid local minimums, which explains the new individulas in the [-3,-10] deflection domain. The optimized design variables are found in table 3 and the optimized deflection is $-25.7°$.

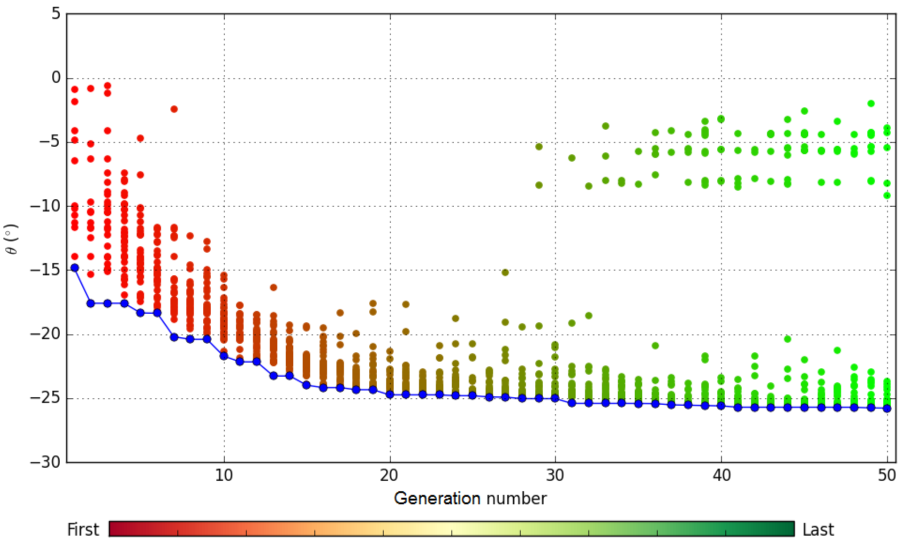

Figure 5: Population throughout the generations in optimization of C_1. The blue line depicts the best individual of each generation.

To better visualize the optimized airfoil and actuators, figure 6 is presented. The module and type of spring are defined via the moment equilibrium without actuation (eq. 20). If the coefficient is negative, it is related to an compression spring; otherwise, it is associated with an extension spring. From equation 20, the spring coefficient is -2443 N/m; hence the

Table 3: Optimized design variables for C_1.

x_s^- (m)	y_s^- (m)	x_s^+ (m)	y_s^+ (m)
-0.068	-0.522	0.153	0.873
x_l^- (m)	y_l^- (m)	x_l^+ (m)	y_l^+ (m)
-0.054	-0.459	0.069	-0.572

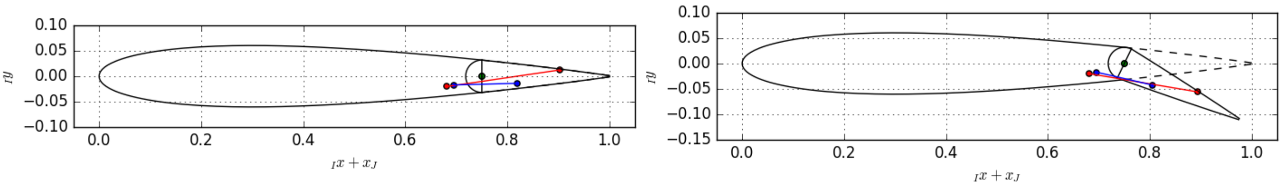

(a) Linear actuator.

(b) SMA actuator.

Figure 6: Schematics of optimized airfoil for C_1 with: (a) no actuation and (b) full actuation.

linear actuator is a compression spring. Although when fully actuated (figure 6b), the actuators almost intersect with the airfoil surfaces, the geometric constraints mentioned in section 2are not violated.

The temperature-driven actuation influences the strains (ϵ_l and ϵ_s), the deflection θ and the forces (F_s and F_l). Figure 7 depicts the influence that temperature has over each of these variables for the *best design* in the optimization. The geometric relation between strains and deflection θ is shown in figure 7a. Because of the non-linear geometric relation, the increase in deflection reduces as both strains becomes less significant. Figure 7b is the result of the constitutive model that couples stress and temperature to obtain strain. Because there is full transformation, the transformation strain ϵ_s^t if fully recovered and no further gain in deflection is possible via heating. Because of the rigid-body coupling, as the SMA strain ϵ_s decreases, the linear strain ϵ_l also decreases. Figure 7c depicts how the force generated by the linear spring and the SMA wire varies with the deflection. Although the curve is quite similar to the curve for ϵ vs. θ (fig. 7a), at small angles the relation differs. At full actuation, the tension at the SMA actuator decreases; hence the elastic component of ϵ_s also decreases during actuation. Since the stroke is the difference between the initial and final actuator lengths, this decrease translates in a higher stroke than a bias configuration with constant stress. Figure 7d is the result of applying the constitutive and the static model. Since thermal expansion is not considered, there is only angle variation during transformation.

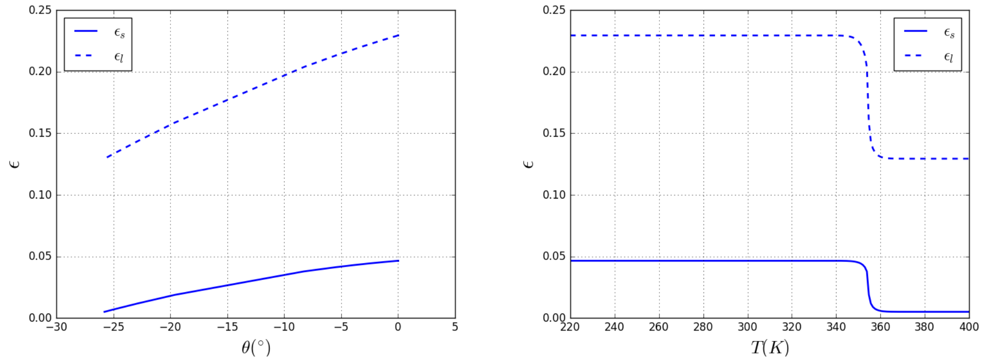

(a) ϵ_s vs. θ

(b) ϵ vs. T

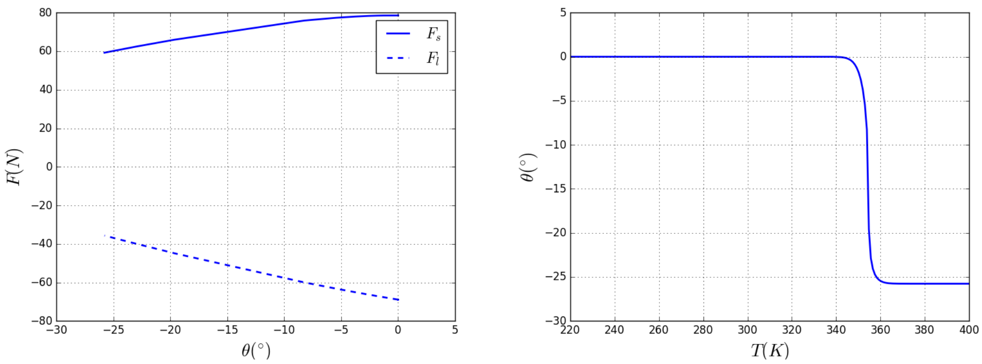

(c) F vs. θ

(d) θ vs. T

Figure 7: Plots of several properties during the static simulation of the airfoil with optimized actuators for C_1.

3.2 Multiobjective optimization

In the previous optimization,without any constraints to k, the optimal solution for C_1 (eq. 21) has a stiffness of 2443 N/m. This high stiffness value is undesirable because the high volume occupied, weight and stress of a spring with high stiffness is undesirable, it is important to reduce k without losing actuation capability. Therefore, for this section, a multiobjective optimization is implemented with the deflection θ and stiffness k as objective functions. Since both θ and k are equally important, a normalized weight sum of the object functions (Grodzevich and Romanko, 2006) with weights equal to 0.5 is used. Thus, the cost function C_2 for the multiobjective optimization is:

$$C_2 = \frac{(1+\bar{\theta}) + |\bar{k}|}{2} \tag{22}$$

where $\bar{\theta}$ and $|\bar{k}|$ are the normalized deflection θ and the absolute spring stiffness $|k|$. To normalize these objective functions, the optimal stiffness of the maximum deflection optimization $|k| = 2443$ and the maximum deflection possible $\pi/2$ are used. Since, the result of the multiobjective optimization will have smaller stiffness coefficients and smaller deflections, the results of the first optimization are used as the baseline.

Utilizing the same static simulation as in the previous subsection, the optimization of cost function C_2 is implemented. All of the individuals analyzed in the optimization, their cost and iteration number are depicted in figure 8. Contrary to the previous optimization, the population followed the same trend minimizing f during the whole optimization, obtaining 0.406 as the minimum value. At the cost of increasing the spring stiffness, higher deflections are obtained. If different values for the cost function weights were utilized, different trade-offs would be obtained. However, the results obtained with the current weights are considered acceptable. The optimized design variables are found in table 4 and the properties of the optimal design are $k = -97.3$ N/m and $\theta = 20.59°$. As with the previous optimization, the optimized linear actuator is a compression spring. Compared to the previous optimized design, the spring stiffness reduced 96%, while there was only a 20% loss in actuation deflection.

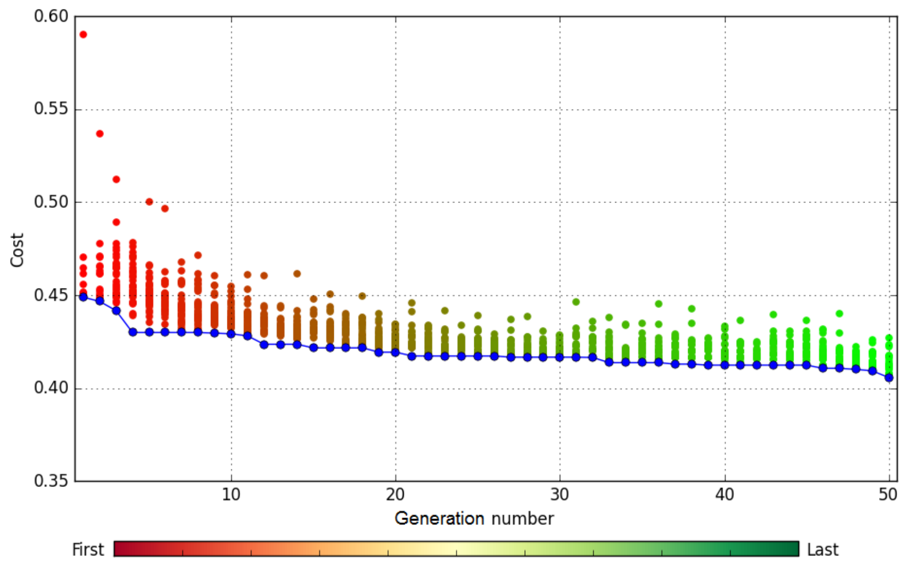

Figure 8: Population and their respective costs C_2 throughout the generations. The blue line depicts the best individual of each generation.

Table 4: Optimized design variables for C_2.

x_s^- (m)	$\bar{y}_s^-$ (m)	x_s^+ (m)	$\bar{y}_s^+$ (m)
-0.125	-0.663	0.123	0.424
x_l^- (m)	$\bar{y}_l^-$ (m)	x_l^+ (m)	$\bar{y}_l^+$ (m)
-0.291	-0.712	0.092	-0.197

The positioning of the actuators for the optimal solution of equation 22 with and without heating are depicted in figure 9. Comparing to the previous actuators (fig. 6), both actuators are longer. To compensate for the smaller stiffness coefficient, higher deformations are necessary to generate enough force to detwinne the SMA. Moreover, the actuators are almost co-linear with and without actuation. This result seems to indicate that co-linear actuators are an interesting configuration to obtain large deflections with low spring stiffness.

The temperature-driven actuation influences the strains (ϵ_l and ϵ_s), the deflection θ and the forces (F_s and F_l). Figure 10 depicts the influence that temperature has over each of these variables. The geometric relation between strains and deflection θ is shown in figure 10a for the *best design* in the optimization. Because of the low spring stiffness, higher

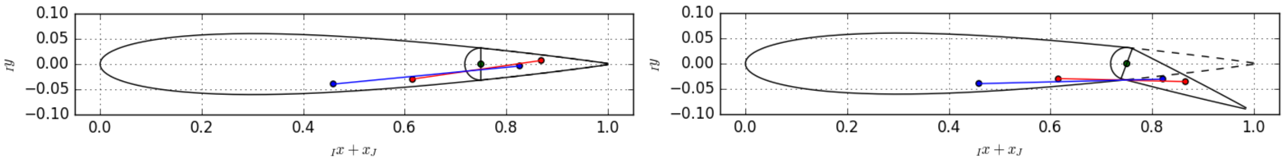

(a) Linear actuator (b) SMA actuator

Figure 9: Schematics of optimized airfoil for C_2 with: (a) no actuation and (b) full actuation.

deformations are necessary to tension the SMA. As a result, the ϵ_l is two orders of magnitude bigger than ϵ_s. Whereas in the previous optimization, they were of the same magnitude. Figure 10b is the result of the constitutive model that couples stress and temperature to obtain strain. Contrary to the previous optimization, full transformation did not happen. Partial transformation took place because the SMA was not heated up to T_{max}. If the SMA were to be heated any further it would violate the maximum deflection constraint defined in subsection 2. Figure 10c depicts how the force generated by the linear spring and the SMA wire varies with the deflection. In the previous optimization, both forces decreased in magnitude as the deflection increased (fig. 7c). Because of the different configuration for the actuator, the moment arm of both actuators varies as a function of θ for the current optimal design differs from the previous. As a results, F_s increases while F_l decreases in magnitude as the SMA is heated. At full actuation, the tension at the SMA actuator increases; hence the elastic component of ϵ_s also increases during actuation. This increase, although small, hinders the actuation stroke. Figure 10d is the result of applying the constitutive and the static model.

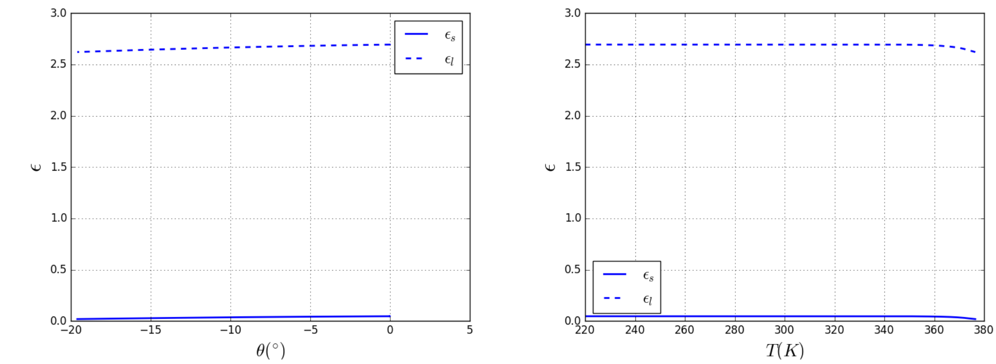

(a) ϵ_s vs. θ. (b) ϵ vs. T.

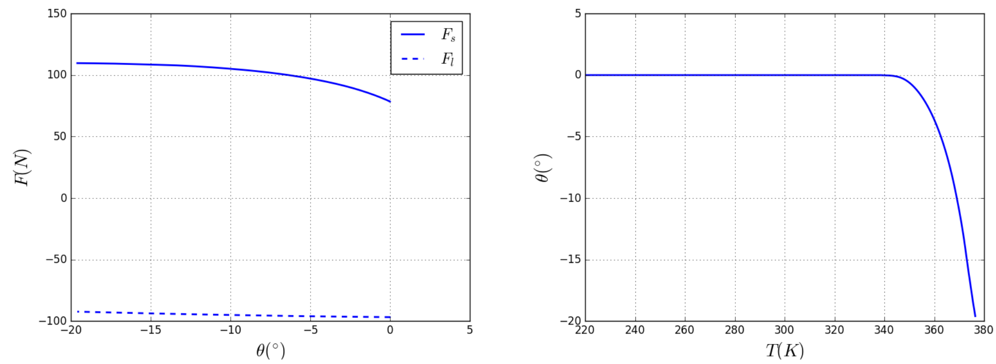

(c) F vs. θ. (d) θ vs. T.

Figure 10: Plots of several properties during the static simulation of the airfoil with optimized actuators for C_2.

4. Conclusions

The static fluid-structure modeling of a flap driven by a bias SMA actuator is proposed, developed and optimized considering different situations. The first optimization determined that the absolute maximum flap deflection in the design herein analyzed is of $25.7°$. The second optimization considered flap deflection and stiffness reduction and determined that it is possible to have a linear actuator with 4% of the spring stiffness of the first optimization, $k = 97.3$ N/m in lieu of the original 2443 N/m, while still having a deflection of $20.6°$ (a 20% decrease). Therefore, SMA wires in a bias configuration can lead to significant flap deflections. Results indicate that a co-linear configuration of both actuators might be ideal for this application. Further work will be focused on optimizing a co-linear configuration, on extending the framework here developed for multi-actuated flaps, on developing a dynamic model to analyze the transient response and on experimentally validating results .

5. Acknowledgements

The authors would like to acknowledge the support of the Brazilian Research Agencies CNPq, CAPES and FAPERJ and through the INCT-EIE (National Institute of Science and Technology - Smart Structures in Engineering) the CNPq and FAPEMIG. The Air Force Office of Scientific Research (AFOSR) is also acknowledged. The authors are grateful to Embraer who supported part of this study. The substantial contribution from Edwin Peraza-Hernandez with the MATLAB constitutive model code is greatly appreciated. The contributions from Eduardo Tancredo and Endryws Moura are also appreciated.

6. REFERÊNCIAS

Abreu, G.L., 2012. "Controle nebuloso aplicado em asas adaptativas utilizando ligas de memória de forma". *Mechanical Engineering Master Thesis (Faculdade de Engenharia, Universidade Estadual Paulista - UNESP)*.

Anderson, J.D., 2011. *Fundamentals of aerodynamics*. Anderson series. McGraw-Hill, New York, 5th edition.

Barbarino, S., Saavedra Flores, E.I., Ajaj, R.M., Dayyani, I. and Friswell, M.I., 2014. "A review on shape memory alloys with applications to morphing aircraft". *Smart Materials and Structures*, Vol. 23, No. 6, p. 063001.

Bellini, A., Colli, M. and Dragoni, E., 2009. "Mechatronic Design of a Shape Memory Alloy Actuator for Automotive Tumble Flaps: A Case Study". *IEEE Transactions on Industrial Electronics*, Vol. 56, No. 7, pp. 2644–2656.

Camara Leal, P., 2016. "AeroPy: An easy to use aerodynamics tool".

Camara Leal, P.B., Bertagne, C.L. and Hartl, D.J., 2015. "Aero-structural Optimization of Shape Memory Alloy-based Wing Morphing via a Class/Shape Transformation Approach".

Deb, K., Pratap, A., Agarwal, S. and Meyarivan, T., 2002. "A fast and elitist multiobjective genetic algorithm: NSGA-II". *Evolutionary Computation, IEEE Transactions on*, Vol. 6, No. 2, pp. 182–197.

Donnelan, Q.A., 2005. "Design and testing of linear shape memory alloy actuator". *Final Report, National Science Foundation–Research Experience for Undergraduates*.

Drela, M., 2001. *XFOIL 6.9 User Primers*. MIT AERO and Astro, Harold Youngren, Aerocraft, Incl.

Elahinia, M.H. and Ashrafiuon, H., 2002. "Nonlinear Control of a Shape Memory Alloy Actuated Manipulator". *Journal of Vibration and Acoustics*, Vol. 124, No. 4, p. 566.

Enemark, S., Savi, M.A. and Santos, I.F., 2014. "Nonlinear dynamics of a pseudoelastic shape memory alloy system - theory and experiment". *Smart Materials and Structures*, Vol. 23, No. 8.

Faria, C.T.d., 2010. "Controle da variação do arqueamento de um aerofólio utilizando atuadores de memória de forma". *Mechanical Engineering Master Thesis (Faculdade de Engenharia, Universidade Estadual Paulista - UNESP)*.

Grodzevich, O. and Romanko, O., 2006. "Normalization and other topics in multi-objective optimization".

Hartl, D.J. and Lagoudas, D.C., 2007. "Aerospace applications of shape memory alloys". *Proceedings of the Institution of Mechanical Engineers, Part G: Journal of Aerospace Engineering*, Vol. 221, No. 4, pp. 535–552.

Ikeda, T., Sawamura, K., Senba, A. and Tamayama, M., 2015. "Shape-retainment control using an antagonistic shape memory alloy system". p. 943117.

Ikuta, K., Tsukamoto, M. and Hirose, S., 1988. "Shape memory alloy servo actuator system with electric resistance feedback and application for active endoscope". In *, 1988 IEEE International Conference on Robotics and Automation, 1988. Proceedings*. pp. 427–430 vol.1.

Kudva, J.N., 2004. "Overview of the DARPA Smart Wing Project". *Journal of Intelligent Materials Systems and Structures*, Vol. 15, No. 4, pp. 261–267.

Lagoudas, D., 2008. *Shape memory alloys: modeling and engineering applications*. Springer, New York, 1st edition.

Lagoudas, D., Hartl, D., Chemisky, Y., Machado, L. and Popov, P., 2012. "Constitutive model for the numerical analysis of phase transformation in polycrystalline shape memory alloys". *International Journal of Plasticity*, Vol. 32-33, pp. 155–183.

Moallem, M. and Tabrizi, V.A., 2009. "Tracking control of an antagonistic shape memory alloy actuator pair". *Control Systems Technology, IEEE Transactions on*, Vol. 17, No. 1, pp. 184–190.

Paiva, A. and Savi, M.A., 2006. "An overview of constitutive models for shape memory alloys". *Mathematical Problems in Engineering*, Vol. 2006, pp. 1–30.

Perez, R.E., Jansen, P.W. and Martins, J.R.R.A., 2012. "pyOpt: a Python-based object-oriented framework for nonlinear constrained optimization". *Structural and Multidisciplinary Optimization*, Vol. 45, No. 1, pp. 101–118.

Ruggiero, M.A.G. and Lopes, V.L.d.R., 1996. *Cálculo numérico: aspectos teóricos e computacionais*. Makron Books, São Paulo.

Schmidt, D.K., 2012. *Modern flight dynamics*. McGraw-Hill, New York, NY.

Senthilkumar, M., 2012. "Analysis of SMA Actuated Plain Flap Wing". *Journal of Engineering Science and Technology Review*, Vol. 5, No. 1, pp. 39–43.

Song, G., Kelly, B. and Agrawal, B.N., 2000. "Active position control of a shape memory alloy wire actuated composite beam". *Smart Materials and Structures*, Vol. 9, No. 5, p. 711.

7. RESPONSABILITY NOTICE

The authors are the only responsible for the printed material included in this paper.